AIAA JOURNAL
Vol. 33, No. 2, February 1995

Structure of a Double-Fin Turbulent Interaction at High Speed

Datta Gaitonde,* J. S. Shang,† and Miguel Visbal‡
Wright Laboratory, Wright-Patterson Air Force Base, Ohio 45433

This study examines the interaction of a Mach 8.3 turbulent boundary layer with intersecting oblique shock waves generated by 15-deg sharp fins mounted symmetrically on a flat plate. The full three-dimensional mass-averaged compressible Navier-Stokes equations are solved with a high-resolution implicit finite-volume scheme. Turbulence closure is achieved with variations of the Baldwin-Lomax algebraic model. Excellent agreement with experimental data is observed for plate surface pressure. However, accurate heat transfer rates are obtained only near the plane of symmetry. Some quantitative details are dependent on the manner in which the turbulence model is implemented. Within this limitation, the overall computed mean flow structure remains similar and mesh independent and compares well with available field surveys. The incoming flat plate boundary layer separates along the entire spanwise width and does not reattach in the domain of computation. Beneath the separated boundary layer are a vortex interaction with an off-surface stagnation point, a centerline longitudinal vortex, and an entrainment flow originating from the essentially inviscid stream near the fin leading edge.

I. Introduction

THREE-DIMENSIONAL shock-wave/turbulent-boundary layer interactions occur commonly in supersonic as well as hypersonic applications. In such flows, the shock wave generated by one surface interacts with the boundary layer generated by an adjacent surface. High-speed three-dimensional turbulent interactions are likely to be ubiquitous in all practical designs for sustained hypersonic flight. The development of such vehicles will rely substantially on computer simulations to reproduce the severe operating environment.

Three-dimensional turbulent interactions are generally studied using relatively simple configurations where the pertaining physics is isolated from the complexity associated with entire aircraft structures. Figure 1, drawn similar to that in Ref. 1, shows one simple geometry that has been the subject of detailed investigation: a sharp wedge mounted on a flat plate. The interaction of the shock wave from the fin with the turbulent boundary layer on the plate results in a three-dimensional turbulent interaction. The principal parameters influencing the flow structure are the Reynolds number, the properties of the incoming boundary layer, the Mach number, and the fin angle (or, alternatively, the normal Mach number). Depending on the values of these parameters, the interaction may be strong enough to induce boundary-layer separation. A review of this research may be found in Ref. 2. The principal flow feature has been determined to be a vortical structure[1] in agreement with the proposal of Kubota and Stollery.[3] The dominant turning action in the flow is counterclockwise when viewed along the vortex axis from the intersection of the fin leading edge (fle) with the plate.

The focus of the present study is a relatively new elementary geometry: the double fin shown schematically in Fig. 2 where two opposed but not necessarily symmetric fins are mounted on the flat plate. The additional relevant parameters introduced are the additional fin angles (or the corresponding shock strengths) as well as an aspect ratio, which may be defined for this vertically semi-infinite fin as the ratio of the spanwise separation distance between the fins to the boundary layer height at the fle. The initial motivation to examine this inlet-like geometry from a theoretical/computational standpoint stems from the observations of Mee and Stalker.[4] Based on experimental data they concluded that, for a given oncoming boundary layer, separation could be inhibited by achieving the desired pressure rise with weaker intersecting shocks as opposed to a single stronger shock. Since boundary-layer separation is undesirable in typical applications, a detailed study of this flow has clear potential practical benefits.

In addition to the flow control aspect of the problem, this geometry can be employed to examine fundamental phenomena in fluid dynamics, particularly 1) the interaction of the two vortical structures induced by the two individual fins and 2) three-dimensional separation in the neighborhood of a symmetry plane. The fluid structures possible due to such events exhibit a high degree of complexity. In this regard, the physics of the problem has relevance in several applications other than inlets. The anticipated vortical structure induced by the right fin is clockwise when viewed along its axis from the intersection of this fle with the plate. The two vortical structures are therefore often designated as opposed or counter-rotating. The turning action of each vortical structure as just described, whether clockwise or anticlockwise, is particular to the observer orientation specified, i.e., viewing into the flow along the axis of each structure. However, these axes are neither coincident nor parallel, and some insight may be gained from consideration in a global reference frame. The symmetry condition on the central plane constrains the streamwise and plate normal components of vorticity to be zero there. However, no such restriction is placed on the spanwise component ω_z which is also unique because it is the only nonzero component of the vorticity in the upstream two-dimensional boundary layer. Thus, vortex lines in the upstream flow form straight lines pointing from the right fin toward the left. In the shock-wave/boundary-layer interaction region, these lines bend and distort but, nevertheless, continue to trace the distance from the right fin to the left and intersect the symmetry plane smoothly along its perpendicular. It is interesting to note that although the present work describes the structure near the symmetry plane as an interaction of two distinct vortices, this continuous aspect of vortex lines in the flow suggests an alternative single structure viewpoint. These vorticity considerations can be related to the large-scale fluid motion due to each vortical structure: a similar rotation is implied by both structures in a plane normal to the spanwise direction. The two primary vortical structures generated by the two fins are thus not opposed in every sense. This aspect is developed in further detail in Sec. III.

The large body of literature on three-dimensional turbulent interactions, especially on the single-fin configuration, indicates that the major portion of the flow away from the solid boundaries is essentially rotational and inviscid.[1] The present effort aims to capture this dominant inviscid portion of the flowfield, especially the wave structure, with a high-resolution scheme based on Roe's flux-difference splitting. Developed primarily for inviscid flows, this upwind-biased

Received March 23, 1994; revision received Aug. 8, 1994; accepted for publication Aug. 15, 1994.

*UES, Inc., Visiting Scientist, Computational Fluid Dynamics Research Branch, Aeromechanics Division. Senior Member AIAA.

†Senior Scientist. Fellow AIAA.

‡Aerospace Engineer, Computational Fluid Dynamics Research Branch, Aeromechanics Division. Senior Member AIAA.

method reveals the favorable blend of numerical properties required to capture details of viscous-inviscid interactions.[5]

Although the effects of viscosity and turbulence are restricted to regions in close proximity to the walls, practical quantitative results, particularly heat transfer rates, are strongly dependent on the manner in which these phenomena are modeled.[6] In this work, turbulence closure is achieved with the method of Baldwin and Lomax (BL). The major drawback with the model is the need to specify a length scale, often a difficult task for complex geometries. For a three-dimensional corner such as that formed by the fin and the plate, the length scale is generally specified by one of two approaches (Sec. II): 1) the Buleev integral (BI) formula (see, e.g., Ref. 7) and 2) the inverse blending (IB) method.[8] Both procedures are employed in this work to assess the sensitivity of the computed flow to variations in eddy viscosity values.

Subsequent to the initial work of Mee and Stalker,[4] the double-fin flowfield has been examined experimentally (e.g., Refs. 9 and 10) as well as numerically (e.g., Refs. 6 and 11). In Ref. 10, Kussoy and Horstman document an extensive experimental effort at Mach 8.3, Reynolds number of 5.3×10^6/m, $\delta = 3.25$ cm, and wall temperature 300 K. Detailed measurements with error estimates are described for the upstream boundary layer, surface pressures, and heat transfer rates as well as surveys of pitot pressure and yaw angle for two sets of symmetrically placed fins in an oncoming stream at a Reynolds number of 5.3×10^6/m. The geometrical details of the present computations duplicate the 15×15-deg configuration. A number of mesh systems are employed to provide an estimate of solution dependence on spatial resolution. In Sec. III, the calculations are first compared with experimental data to validate the solution. The subsequent examination of mean flow structure is divided into kinematic and dynamic features.

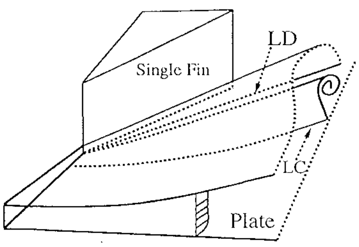

Fig. 1 Flowfield structure for single-fin configuration showing line of coalescence (LC) and line of divergence (LD).

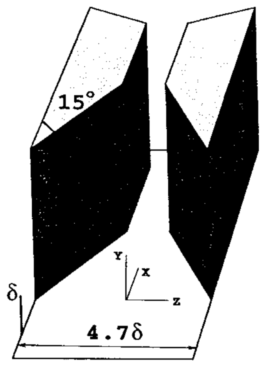

Fig. 2 15×15 double-fin configuration.

II. Theoretical Model

The three-dimensional mass-averaged compressible Navier-Stokes equations are solved in strong conservation form on a curvilinear coordinate system. Details of the solution procedure may be found in Ref. 12 and are only briefly summarized here. The inviscid fluxes are discretized with Roe's flux-difference split scheme implemented in a cell-centered finite-volume formulation with the monotonic upwind-centered scheme for conservation laws (MUSCL) reconstruction approach of van Leer.[13] Monotonocity is enforced with a harmonic limiter, and an appropriate cutoff is employed to satisfy the entropy condition. Time integration is achieved with an implicit residual driven line Gauss-Seidel relaxation scheme requiring the solution of a series of block tridiagonal systems, one for each line normal to the plate.

The viscous fluxes in the Navier-Stokes equations are discretized with centered differencing. The BL turbulence model is employed to incorporate the effects of turbulence through the eddy viscosity assumption. The implementation of the model is ambiguous in the vicinity of a corner such as at the juncture of the fin and the plate. In this work, two procedures are investigated. The principal distinction between these is in the specification of an appropriate length scale. In the BI approach, the formula of Buleev for an open corner as described in Ref. 7 is employed. In the IB procedure, the length scales and the eddy viscosity values at any point are obtained by considering the effect of the plate and the fin independently. The two values so obtained at each point are then blended with an appropriate function depending inversely on the distance to each surface.[8]

The condition of symmetry is invoked on the central plane and, thus, only one-half the domain of the experiment is calculated. For the configuration examined by Kussoy and Horstman,[15] the fins end abruptly. To simulate any effects of the trailing-edge expansion on the computed solution, a 45-deg duct is appended to the end of the domain.

Boundary conditions are specified for the explicit as well as the implicit portion of the algorithm. On both solid surfaces (fin and plate), the no-slip condition is enforced, the wall temperature is specified based on experimental data (300 K), and the normal pressure gradient is assumed to be zero. The boundary layer on the fin is considered to be fully turbulent from the leading edge. At the upstream end of the domain, the momentum thickness of the incoming boundary-layer profile is matched with the experimental value ($\theta = 0.083$ cm at the fle). This profile is generated independently with a two-dimensional boundary-layer code based upon the BL model.[14] The downstream and top boundaries are assumed to be far enough away for the application of simple zero-gradient extrapolation to be valid. Symmetry conditions are imposed on two planes, one upstream of the fin leading edge and the other equidistant between the two fins. In the absence of any qualification, the term symmetry plane refers to the latter.

The grid is generated as a sequence of nonuniform Cartesian planes normal to the direction of the upstream flow. In each plane, the grid is clustered in the vicinity of the solid boundaries to provide adequate resolution of the boundary layer. Calculations are described on two mesh systems whose properties are noted in Table 1. The first, designated C (meshes A and B are subsets employed primarily to accelerate convergence through grid sequencing) is designed to conservatively satisfy the constraints of Ref. 7. Calculations with both the Buleev integral as well as the inverse blending procedure are described on this mesh. A finer mesh, denoted E (D being a subset of E) provides not only an estimate of so-

Table 1 Grid size and mean spatial resolution

Mesh	$IL^a \times JL^b \times KL^c$	$\Delta x/\delta^d$	$\Delta y/\delta$	$\Delta z/\delta$	MD^e($/\delta^3$)	Δy^{+f}	Δz^+
C	$84 \times 82 \times 66$	0.25	2.5×10^{-2}	2.4×10^{-2}	2378	1.0	0.5
E	$106 \times 80 \times 81$	0.16	3.3×10^{-3}	1.47×10^{-2}	6654	1.4	0.8

[a] $IL/\Delta x$ = streamwise points/spacing.
[b] $JL/\Delta y$ = plate-normal points/spacing.
[c] $KL/\Delta z$ = spanwise points/spacing.
[d] $\delta = 3.25$ cm.
[e] MD = mesh density (points per volume).
[f] superscript + = wall units of first point from wall.

lution dependence on mesh resolution but also higher fidelity of certain regions where interesting flow features were detected on mesh C. This includes mainly the region of vortex interaction near the symmetry plane. Convergence is determined for all computations by monitoring several quantities, including the residual of the solution vector, surface pressure and heat transfer rates, as well as integrated root mean square measures of several quantities on the plate.[12]

III. Results

Validation of Computed Results

Experimental surface pressure and heat transfer rate measurements are available[10] along the centerline and at three crossflow stations whose locations are exhibited in Fig. 3. Note that the locations of the spanwise measurements of heat transfer rates are not coincident with those for the pressures. For the purposes of the following discussion, the freestream shock structure in terms of pressure contours is presented in the top portion of the figure. The inviscid structures primary shock (PS), shoulder expansion (SE), and several reflected shocks (RS1–RS3) are marked. The inviscid method captures these shocks very accurately, typically over one cell and without any spurious oscillations. The pressure distribution on the plate surface is shown in the lower portion of the figure. Near the symmetry plane, the increase in pressure in the central region is much more rapid than near the fins. These features will be examined in detail in a later section.

The computed and experimental variation in pressure ($P = p/p_\infty$) along the centerline is shown in Fig. 4. The 10% error estimates for the experimental values are marked as specified in Ref. 10. Computed values on mesh C are plotted with both the BI and the IB procedures whereas only the latter is examined on mesh E. All calculations capture the qualitative variation observed experimentally. The initial pressure rise, often employed as a measure of upstream influence, occurs slightly beyond $X = x/\delta = 2$, x being measured from the fle. Peak pressures occur at about $X = 6.5$, downstream of the intersecting shocks. The subsequent drop in pressure is associated with the relief effect of the expansion emanating from the fin shoulder. Although the pressure in the inviscid region achieves the theoretical value across shocks PS and RS1 ($p_2/p_\infty \sim 45$), the peak surface pressure is significantly lower than the inviscid asymptote. In addition, the conspicuous plateau region observed in single-fin calculations is absent on the symmetry plane. The calculated results predict a more rapid rate of increase in the initial portion of the interaction than observed experimentally. Nevertheless, outside of the region $5 < X < 7$ where modest disagreement is observed, the calculations with the IB model fall within the bounds of experimental data. In contrast, significant overprediction is evident with the BI method in the regions of high local pressure. The agreement between computed and experimental spanwise surface pressure profiles at the three stations is comparably good and may be found in Ref. 12.

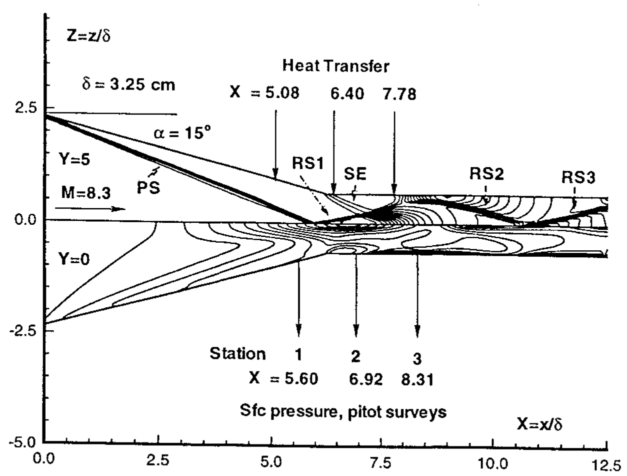

Fig. 3 Locations of experimental surveys; computed shock structure on mesh E with pressure contours, freestream on top, plate at bottom.

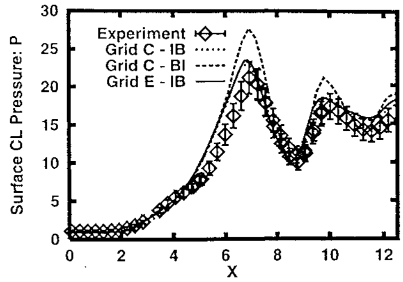

Fig. 4 Streamwise variation of surface pressure along the centerline, $P = p/p_\infty$, $X = x/\delta_\infty$.

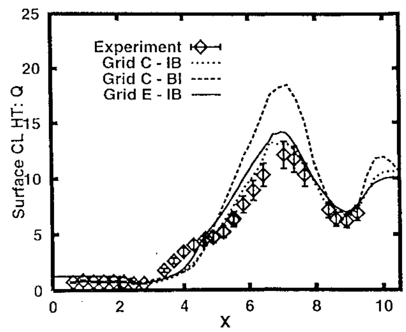

Fig. 5 Streamwise variation of heat transfer rate along the centerline, $Q = q/Q_{\mathrm{expt}}$, $Q_{\mathrm{expt}} = 10{,}400$ W/m^2, $X = x/\delta_\infty$.

The heat transfer rates along the centerline (Fig. 5) follow the same qualitative variation with streamwise distance as pressure. The ordinate Q is the heat transfer normalized by the value utilized by the experimentalists in their data presentation. All calculations exhibit an initial decline at $X \sim 2$, reflected to a lesser extent in the experimental data also where uncertainty is 10%. This is possibly caused by flow separation. The subsequent rise in heat transfer occurs more rapidly in the calculations but at a slightly farther downstream location than in experiment. Once again, the BI procedure overpredicts the values of heat transfer over the entire domain whereas the IB method performs considerably better. As noted earlier, the distinction between the two methods is most crucial in the specification of the length scale. In the BI method, the influence of the corner is directly modeled into the length scale employed to compute the eddy viscosity. In this work, the asymptotic open corner form of the Buleev length scale is employed. This may be a source of inaccuracy since near the center of the interaction, the influence of both fins is presumably comparable because of symmetry but is not modeled. More sophisticated versions of this length scale are available and may improve the accuracy. In the IB method on the other hand, the effect of the corner is modeled at a later stage in the eddy viscosity calculation. Near the centerline, the independent contribution of the eddy viscosity due to the fin is negligible because of the rapid decline caused by the intermittency correction in the outer formulation of the BL model. Thus, the effect of the corner diminishes more rapidly in the IB method, leading to a more localized evaluation of the eddy viscosity. Near the plate, these values are generally lower than with the BI method, and lower local heat transfer rates are observed.

Off-centerline, the heat transfer comparison between calculation and experiment deteriorates quite rapidly with both methods at each of the three locations of Fig. 3. This is typified in Fig. 6 exhibiting the comparison at $X = 6.4$. The lowest rates are observed near the corner of the fin and the plate. The calculations overpredict the heat transfer rates at nearly all points. The comparison becomes worse at the farthest downstream location $X = 7.78$ (not shown) although a modest advantage falls to the IB approach. Similar large discrepancies with heat transfer data have been observed by other workers[6] and are thought to be associated with deficiencies in turbulence modeling.

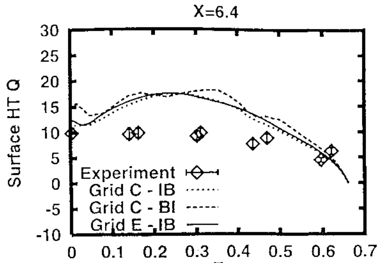

Fig. 6 Spanwise variation of heat transfer rate at X = 6.4, $Q = q/Q_{\text{expt}}$, Q_{expt} = 10,400 W/m², $Z = Z/\delta_\infty$.

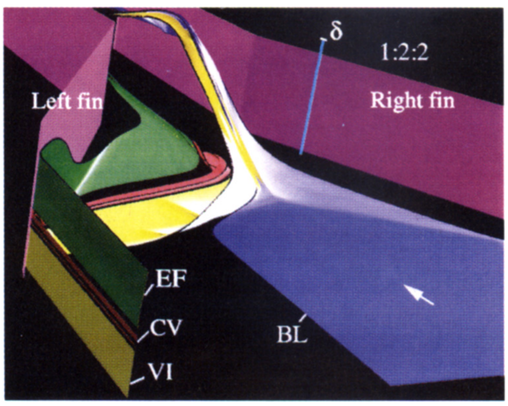

Fig. 7 Structure of flow: stream ribbons on mesh E showing boundary layer (BL), vortex interaction (VI), centerline vortex (CV), and entrainment flow (EF).

The effect of increased mesh resolution may be assessed with Figs. 4–6. In each of these figures, it is evident that the two calculations with the IB method on meshes C and E agree very well with each other qualitatively as well as quantitatively. Despite the discrepancies with heat transfer data, differences in details of mean flow structure between the two meshes as well as the two models are negligible. For example, all calculations demonstrate separation of the fin boundary layer beyond the shoulder (not shown). The size and location of this feature are in good agreement with the experimental data. These observations lead to conclusions similar to those made in Ref. 1 for the single fin: the effect of turbulence and its modeling is restricted to regions close to walls whereas the remaining dominant portion of the flowfield is unaffected by sizable eddy viscosity variation. The comparison of flowfield data with experimental pitot pressure surveys provides significant insight into the flow structure and is presented later.

Kinematic Aspects of Flow Structure

Several of the figures presented are plotted with artificial aspect ratios as marked (x : y : z) to highlight features under discussion. For the same reason, the height of the fin is often truncated and a length scale is provided by the upstream boundary-layer thickness. Following the terminology of Ref.15, the term vortex is used interchangeably with vortical structure, both implying helical type of motion about a three-dimensional axis.

The flowfield structure is exhibited in Fig. 7 with sequences of particle traces whose trajectories pass in the proximity of lines of accumulation on the computed surface flow pattern which is discussed subsequently. The salient features of the computed mean flow structure may be summarized as follows.

Separated boundary layer: The entire oncoming turbulent boundary layer (marked BL in Fig. 7) separates through the formation of a line of coalescence on the plate. The height of fluid following this trajectory varies from small near the fle to large on the symmetry plane. The surface formed by the separating boundary layer is broad upstream, extending from one fin to the other (a portion near the left fin has been cut away in Fig. 7). However, because of the higher sweep angle of the particles near the fins, the width of this surface is considerably smaller downstream. This layer does not reattach to the plate in the domain of computation thus setting up an open flow structure without any recirculation or dead air region. The region beneath this separated layer is occupied by spanwise movement of fluid from various heights in the boundary layer near the fle.

Vortex interaction (VI): The flow attaching immediately downstream of the separated boundary layer originates from a relatively close distance to the plate near the fle. The two streams, one from each fin, exhibit a vortex interaction on the symmetry plane. This is characterized by reversed flow and an off-surface stagnation point.

Centerline vortices (CV): Particles from slightly higher locations in the boundary layer near the fin also traverse the spanwise distance to the symmetry plane. However, the two streams from either side are subsequently turned in the streamwise direction to form two relatively small counter-rotating vortical structures close to the plate. The rotation of each of these vortices is also counter to that of the entrainment flow (described next) on the same side of the plane of symmetry.

Entrainment flow (EF): A helical-type flow, originating in the essentially inviscid region, occupies the region below BL and VI and entrains high energy fluid into the interaction. The axis of this turning motion as well as that of the secondary vortex are roughly streamwise aligned.

In addition to these features, a corner vortex similar to that observed in single-fin flow is also evident but is not examined in much detail because of its relative insignificance to the dynamics of the interaction. The described structure is now elucidated by examining limiting and select three-dimensional streamlines.

The experimental and computed (mesh E) surface streamline patterns are shown in Figs. 8 and 9, respectively. The former shows the salient directions deduced by the experimentalists[10] since surface oil flow patterns do not reproduce well. Several of the important features are marked in the calculated result. It should be noted that mesh C shows the same pattern with both implementations of the turbulence model. The computed pattern exhibits a line of coalescence [denoted principal line of separation (PLS)] extending the entire spanwise distance from one fin to the other. Very close to the fin, a line of divergence [denoted principal line of attachment (PLA)] is evident. This line remains very close to the fin until the shoulder after which it shows a wavy pattern. A second line of coalescence (denoted secondary line of separation (SLS)] is formed close to and roughly parallel to the centerline. This line is evidently distinct from that associated with primary separation. Finally, a second line of divergence is visible on the centerline [denoted center line of attachment (CLA)]. The lines SLS and CLA approach each other as they move downstream.

These particular lines are connected and related to each other through a sequence of critical points, i.e., surface locations at which the shear stress is zero. For a classification of critical points, see Ref. 16. Figure 10 is an enlarged view of the surface streamline structure (black) near the centerline. The blue lines are surface vortex lines whose structure is discussed later. Four critical points are observed: node of separation (NS), node of attachment (NA), and saddle point (SP) (one on either side of the symmetry plane). These points form a roughly diamond-shaped pattern. Sufficient numerical definition is assured by a reasonable mesh density in this area. Nodes NS and NA are located along the centerline at distances of 2.4δ and 4.5δ from the fle, the region in between being resolved with 14 points in the streamwise direction for mesh E. The two SPs are located at 3.1δ from the fle, the distance of each to the symmetry plane (0.2δ) is resolved by 14 points in the spanwise direction.

The two PLSs arising from each fin terminate at NS which is a stable (or attracting) node. SLS forms downstream of the SP. A region containing these critical points exhibits reversed flow. The segment of the separatrix joining the SP with the PLA is significant for reasons to be outlined later and is, therefore, indicated separatrix

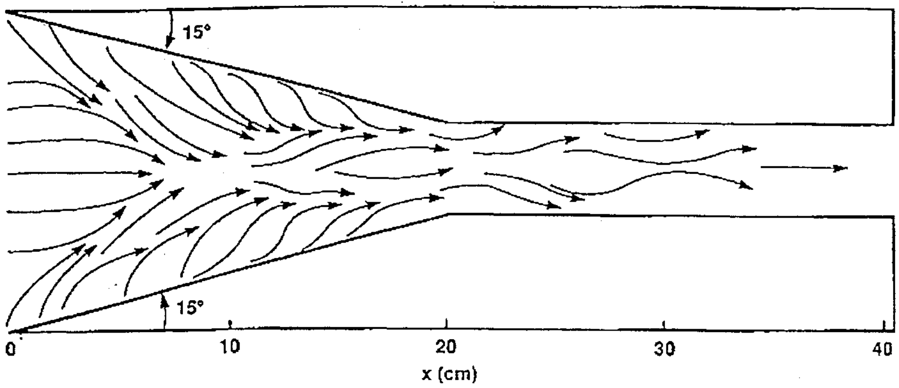

Fig. 8 Experimental sketch of skin friction lines.[10]

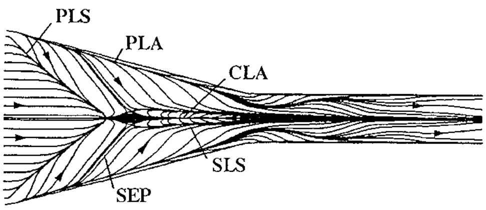

Fig. 9 Computed surface streamline structure on mesh E.

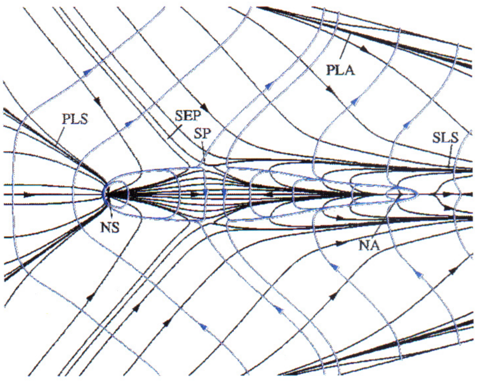

Fig. 10 Critical point structure near centerline: surface vortex lines in blue and surface streamlines in black.

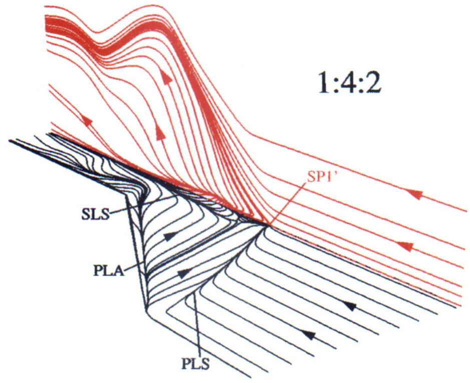

Fig. 11 Streamlines on symmetry plane (red) with plate surface streamlines in black.

(SEP) in Figs. 9 and 10. Although the presence of each of the lines PLS, PLA, SLS, and CLA can be inferred in the experimental result (Fig. 8), the local critical point structure is not. A precise comparison for the locations of each particular line introduced in Fig. 9 is not feasible. However, in the region where the PLS is nearly straight, a rough estimate may be made of the angle with the streamwise direction. The agreement is good: 40 deg in the experiment and 38 deg in the calculation on mesh E.

Garrison and Settles[17] have proposed a flow model based on several experiments at Mach 3 and Mach 4. They describe flow bifurcation with increasing fin angle. The present pattern most resembles their strongest interaction. Although the Mach numbers examined in Ref.17 are significantly lower, previous computational results[6] have concluded that the overall mean flow structure remains similar at the higher Mach numbers considered in this work. Several features are common: PLS, PLA, CLA and NA, denoted in Ref. 17 as primary separation (PS), primary attachment (PA), centerline attachment (CA), and node of attachment (NA). The critical point NA is not actually observed but is postulated to satisfy topological constraints of an upstream centerline saddle point. Their saddle-node structure and the associated bubble separation is clearly distinct from the node-saddle-node combination and corresponding open three-dimensional separation in the present calculation. One other noteworthy difference is in the origin of the line representing secondary separation; in the present work this becomes visible downstream of the saddle point whereas in the proposal of Ref. 17 it originates farther upstream, close to the fle.

Further light may be shed on the structure of the flowfield by examination of the streamlines in the symmetry plane. These are depicted in Fig. 11 in red, along with the surface streamlines on the plate in black. One interesting observation is that the separating streamline on the symmetry plane does not reattach in the computational domain and there is no closed two-dimensional bubble in the computed flow. Rather, the flow underneath the separating streamline is occupied by that arriving from the spanwise direction. Figure 12 exhibits the structure in the vicinity of the critical points on the plate. It is observed that the nodes NS and NA on the plate appear as half-saddles of separation (SP1') and attachment (SP2'), respectively, on the symmetry plane. In addition, another critical point occurs within the flow. This unstable (i.e., repelling) focus (UF') is representative of the vortex interaction of the two structures arriving on the symmetry plane from either side. The sense of rotation about UF' is the same as that of the vorticity in the upstream two-dimensional boundary layer. This stagnation point is located very close to the plate ($0.02\delta \sim 0.7$ mm), the distance to the plate is resolved with 13 points. Despite the close proximity of UF' to the plate, all streamlines below the shear layer formed by the separated boundary layer and the vortex interaction emanate from UF'. The height of this shear layer eventually exceeds 1δ downstream. The fluid in the vortex interaction thus occupies a relatively large region on the plane of symmetry and actually originates from near the fle in the upstream flow. A line of bifurcation (LB') emanates from UF', the flow on the lower portion attaches to the plate downstream of NA along the CLA, and it is entrained into the secondary vortex.

A few comments on this topological structure are in order. First, the number and types of critical points possible are related through a set of topological laws (see, for example, Ref. 16). The summation of critical points on both the plate and the symmetry plane satisfies these laws. Second, strong evidence of the possible existence of this topology is presented by Dallmann[15] who has examined the features of steady three-dimensional vortex structures in the neigh-

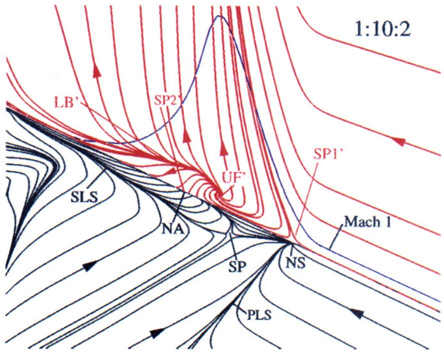

Fig. 12 Expanded view of streamlines on symmetry plane.

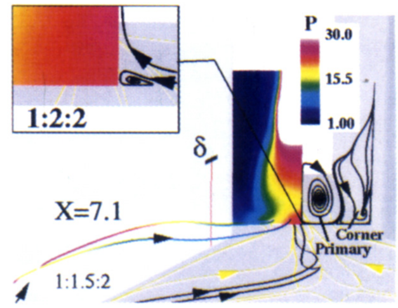

Fig. 13 Pressure and sectional streamlines in the X = 7.1 plane.

borhood of symmetry planes. The behavior described in Figs. 10 and 12 is precisely one possible elementary structure evolving as a result of flow bifurcation from a degenerate critical point. The surface vorticity topology (shown blue in Fig. 10) agrees with that presented in Ref. 15. As anticipated, these lines are orthogonal to the surface streamlines and proceed from the right fin to the left, intersecting the centerline along a normal. Centers are observed at NS and NA whereas the saddles in the surface streamline pattern remain unaltered. Finally, although the entire structure lies in the subsonic region (see Fig. 12), it is nevertheless important to note that the analysis of Ref. 15 is focused on features of divergence-free velocity fields. In addition to uncertainties caused by compressibility, the details of this structure may depend on the turbulence model employed. In Ref. 6, no critical points are evident with a two-equation model though a node-saddle combination (the node being similar to that marked NS) is observed with the Baldwin-Lomax model.

The previously described structure of three-dimensional separation on the symmetry plane is distinct from that observed on the symmetry plane upstream of a juncture flow.[18] In both instances, the boundary conditions are those dictated by symmetry. However, in a laminar juncture flow, fluid moves away from the symmetry plane as it flows around the body and the foci of vortex structures in this plane are stable. In the double-fin flow, on the other hand, fluid approaches the symmetry plane and the single observed focus is unstable. The motion of fluid toward or away from the symmetry plane also has significant consequences on the critical point structure on the plate. For the juncture flows described in Ref. 18, the foremost critical point on the plate centerline is a saddlepoint. The separatrices of such a saddle point are constrained by symmetry to lie orthogonal to each other: one along the centerline (fluid approaching), the other perpendicular to it (fluid leaving). In the double-fin configuration, fluid approaches the foremost centerline critical point on the plate not only from upstream but also from the sides. This precludes a foremost centerline saddle point and hence the observed node NS.

The mean flow structures presented in Fig. 7 may be correlated with the patterns observed on the plate and symmetry plane. The fluid adjacent to the plate in the oncoming boundary layer separates at the PLS, the region underneath being occupied by the spanwise movement of the flow attaching at the PLA. The portion of the flow whose footprint lies between the PLS and the separatrix SEP (Fig. 9) separates from the downstream side of the PLS and is swept near the symmetry plane into the vortex interaction described by the focus UF' and the two saddle points SP1' and SP2' (Fig. 12). Some fluid flowing over the SLS is turned by the symmetry plane and forms the streamwise-aligned secondary vortex (marked CV in Fig. 7) the sense of rotation of which is counter to that formed by the motion of the entrainment flow. The region between the SLS and the CLA is occupied near the plate by this centerline vortical structure. A comparison with the experimental flow footprint of Fig. 8 seems to indicate computational underprediction in the spanwise extent of this feature. The development of the separation surface emanating from the SLS effectively restricts the total amount of fluid in the secondary vortex and the two SLSs from each side of the symmetry plane asymptote with the CLA. The entrainment flow (see Fig. 7) attaches at larger distances downstream of the fin leading edge, traverses the spanwise length of the domain, and separates at the SLS.

Further evidence of the existence of the centerline vortex is revealed in restricted particle traces at section $X = 7.1$ as shown in Fig. 13 where they are plotted on the right side of the plane of symmetry viewing downstream. The spatial relationship of the various features with the surface pattern is exhibited by a limited set of surface traces (yellow) as well as stagnation pressure colored three-dimensional streamlines representative of the different flow features identified earlier. The static pressure contours also displayed will be utilized for the discussion on flow dynamics presented later. Three rotating structures are observed on each side of the symmetry plane. The focus closest to the fin is due to the corner vortex which shows a large increase in dimension beyond the shoulder. The central focus, denoted primary, consists of fluid in BL and VI in the upper portion and EF below. Close to the plate (see inset in Fig. 13), the trace of the centerline vortex is also visible. The sectional streamline topology near the symmetry line bears resemblance to that proposed in Ref. 17. Viewing downstream along the axis of each vortical structure due to the right fin, the turning implied by both the corner and centerline vortices is counter-clockwise whereas that due to the primary/entrainment structure is clockwise. The dimensions of the various features presented are likely dependent on the relevant flow parameters particularly Mach number and aspect ratio.

Dynamic Aspects of Flow Structure

The penetration of the inviscid shock into the boundary layer occurs through compression fans that are often described as forming a λ pattern (e.g., Ref. 2). For the three-dimensional interaction due to the single fin, and also in the double fin for short distances downstream of the fin leading edge, this structure is observed on both streamwise and spanwise planes. Thus, near each fle, a diffuse pressure rise exists on the plate in the streamwise direction reflecting sizable upstream influence of the shock wave (Fig. 3). This gradient is sufficient in the present instance to cause separation of the low energy fluid in the boundary layer. In the inviscid region constituted by high energy particles, the streamwise static pressure gradient gradually sharpens whereas the upstream influence diminishes. As a result, downstream of the primary shock, the static pressure is higher in the essentially inviscid region than on the plate. The downward motion of the entraining flow generally follows the favorable pressure gradient in this direction. Similarly, away from the symmetry plane, the spanwise component of pressure gradient on the plate is favorable for fluid to move toward the centerline.

The dynamics of the flow near the centerline does not have a direct relationship with that for a single-fin interaction. The computed and experimental pitot pressures at station 1 (see Fig. 3) are plotted in Fig. 14. Note that the experimental data does not extend to the surfaces. The overall agreement between calculation and experiment is very good, both qualitatively as well as quantitatively. The size and shape of the roughly circular region of low pitot pressure in the center of the domain are accurately reproduced. The comparison with data at stations 2 and 3, especially the region of low pitot pressure, is similar and is not shown for brevity (see Ref. 12). At each of these sections, the central portion of the interaction is also a low-energy region. This is illustrated in Fig. 15,

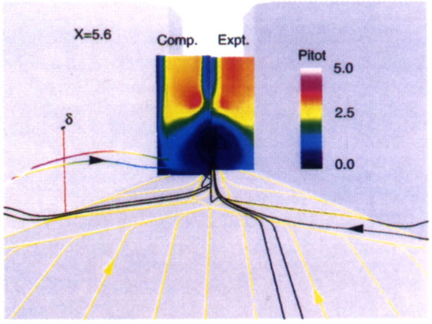

Fig. 14 Pitot pressure comparison with experiment: station 1, X = 5.6.

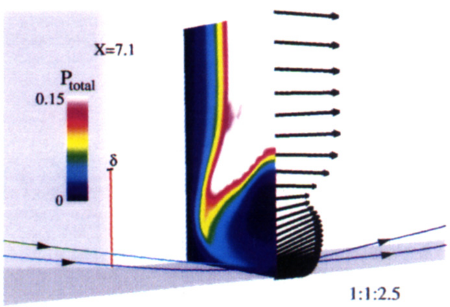

Fig. 15 Total pressure normalized by freestream value on X = 7.1 and velocity profile on symmetry plane.

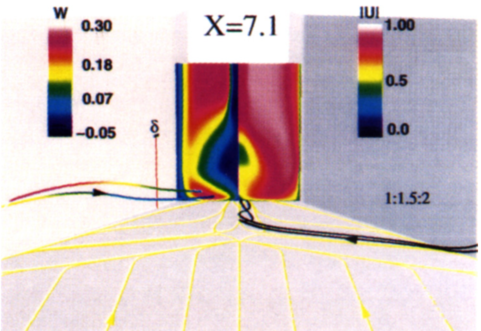

Fig. 16 Velocity on X = 7.1 plane: spanwise component on left and total velocity on right.

which shows the total pressure at a streamwise location $X = 7.1$. The range of total pressure values plotted in this figure corresponds to that in the lower-half of the upstream boundary layer. This low energy fluid is mainly composed of particles whose trajectories pass through regions close to the PLS, i.e., the low-energy fluid in the separated upstream boundary layer as well as the vortex interaction flow. On the plane of symmetry, the shear layer constituted by these two streams occurs in the upper portion of the low-energy region.

Figure 14 also exhibits the turning motion of the high-energy entrainment flow composed of particles originating relatively high in the boundary layer. These exhibit a large sudden drop in stagnation pressure across the primary shock and then a gradual decline as they move through the system of compression fans with adverse streamwise pressure gradient toward the symmetry plane where they meet with fluid in the centerline counter-rotating vortex. On the symmetry plane, this high-energy entrainment flow enhances the streamwise component of the velocity near the plate. This is exhibited in Fig. 15 which shows the symmetry plane velocity vectors at section $X = 7.1$. A wake-like profile is observed in which the high velocities near the plate and in the inviscid freestream bound the low-energy, low-velocity fluid in the central portion constituted principally by the vortex interaction flow.

A final observation concerns the high static pressure observed near the centerline close to the plate. This is evident in Fig. 13 introduced earlier in reference to the kinematic structure of the flow. The phenomenon has been observed in previous computational[6] and experimental observations.[9] The earlier described flow structure suggests a plausible mechanism and is outlined with reference to Fig. 16 exhibiting the spanwise (left) and total (right) velocities in the $X = 7.1$ plane. As mentioned previously, the fluid in the entrainment flow experiences a large increase first in the downward and then in the spanwise components of velocity. At short distances off the symmetry plane, this spanwise component is sizable and positive (Fig. 16) indicating a wall-jet like supersonic flow impinging on the symmetry plane which from kinematic considerations alone must turn the fluid in the streamwise direction. This effectively stagnates the fluid velocity component in the spanwise direction, resulting in the observed region of relatively high static pressure near the plate centerline. Additionally, the pressure distribution so created constitutes an adverse gradient to the entrainment flow which is then sufficient to cause separation of the fluid near the plate surface, i.e., the separation associated with SLS.

IV. Conclusions

The flowfield due to the interaction of a turbulent boundary layer with symmetric intersecting shocks at Mach 8 is examined with a high-resolution method. The validation with experimental data is generally good with the exception of heat transfer rates off centerline. An examination of the mean structure of the flow reveals many distinct features. The surface pattern shows several lines of accumulation connected by critical points. Near the centerline, a theoretically predicted elementary bifurcation is observed. The flowfield is discussed in terms of kinematic and dynamic features. The computed flow reveals the existence of a three dimensionally separated boundary layer with no recirculation region. A vortex interaction is evident underneath, characterized by reversed flow and a stagnation point in the symmetry plane. Two small opposed streamwise-aligned centerline vortices are formed on either side of the symmetry plane. These are also individually opposed to the larger helical motion demonstrated on the same side of the plane of symmetry by an entrainment flow originating from the essentially inviscid region near the fin leading edge.

Acknowledgments

These calculations were performed on computers operated by NAS and Kirtland AFB and were analyzed at Wright-Patterson AFB. The permission of M. Kussoy to reproduce Fig. 8 is acknowledged.

References

[1]Knight, D., Horstman, C., Shapey, B., and Bogdonoff, S., "Structure of Supersonic Turbulent Flow Past a Sharp Fin," *AIAA Journal*, Vol. 25, No. 10, 1987, pp. 1331–1337.

[2]Settles, G. S., and Dolling, D. S., "Swept Shock/Boundary-Layer Interactions: Tutorial and Update," AIAA Paper 90-0375, Jan. 1990.

[3]Kubota, H., and Stollery, J., "An Experimental Study of the Interaction Between a Glancing Shock Wave and a Turbulent Boundary Layer," *Journal of Fluid Mechanics*, Vol. 116, 1982, pp. 431–458.

[4]Mee, D., and Stalker, R., "Investigation of Weak Shock-Shock and Shock-Expansion Intersection in the Presence of a Turbulent Boundary Layer," AIAA Paper 87-0549, Jan. 1987.

[5]Gaitonde, D., and Shang, J., "Accuracy of Flux-Split Algorithms in High-Speed Viscous Flows," *AIAA Journal*, Vol. 31, No. 7, 1993, pp. 1215–1221.

[6]Narayanswami, N., Horstman, C. C., and Knight, D. D., "Numerical Simulation of Crossing Shock/Turbulent Boundary Layer Interaction at Mach 8.3—Comparison of Zero- and Two-Equation Turbulence Models," AIAA Paper 93-0779, Jan. 1993.

[7]Knight, D. D., "A Vectorized Three-Dimensional Navier-Stokes Code for High Speed Inlets," Rutgers Univ., Tech. Rept. RU-TR-161-MAE-F, New Brunswick, NJ, 1983.

[8]Chen, C.-L., and Hung, C.-M., "Numerical Study of Juncture Flows," *AIAA Journal*, Vol. 30, No. 7, 1992, pp. 1800–1807.

[9]Garrison, T. J., and Settles, G. S., "Flowfield Visualization of Crossing Shock-Wave/Boundary Layer Interactions," AIAA Paper 92-0750, Jan. 1992.

[10]Kussoy, M. I., and Horstman, K .C., "Intersecting Shock-Wave/Turbulent Boundary Layer Interactions at Mach 8.3," NASA TM-103909, 1992.

[11]Gaitonde, D., and Knight, D., "Numerical Investigation of Some Control

Methods for 3-D Turbulent Interactions Due to Sharp Fins," AIAA Paper 89-0360, Jan. 1989.

[12]Gaitonde, D., and Shang, J. S., "Calculations on a Double-Fin Turbulent Interaction at High Speed," AIAA Paper 93-3432, Aug. 1993.

[13]van Leer, B., "Towards the Ultimate Conservation Difference Scheme V, A Second-Order Sequel to Godunov's Method," *Journal of Computational Physics*, Vol. 32, 1979, pp. 101–136.

[14]York, B., "Evaluation of the Baldwin-Lomax Turbulence Model for a Class of Boundary Layer Flows," M. S. Thesis, Mechanical and Aerospace Engineering Dept., Rutgers Univ., New Brunswick, NJ, 1984.

[15]Dallmann, U., "Three-Dimensional Vortex Structures and Vorticity Topology," *Fluid Dynamics Research, The Japan Society of Fluid Mechanics*, Vol. 3, 1988, pp. 183–189.

[16]Tobak, M., and Peake, D. J., "Topology of Three-Dimensional Separated Flows," *Annual Review of Fluid Mechanics*, Vol. 14, 1982, pp. 61–85.

[17]Garrison, T. J., and Settles, G. S., "Interaction Strength and Model Geometry Effects on the Structure of Crossing-Shock Wave/Turbulent Boundary-Layer Interactions," AIAA Paper 93-0780, Jan. 1993.

[18]Visbal, M. R., "Structure of Laminar Juncture Flows," *AIAA Journal*, Vol. 29, No. 8, 1991, pp. 1273–1282.